41st AIAA Fluid Dynamics Conference and Exhibit
27 - 30 June 2011, Honolulu, Hawaii

AIAA 2011-3079

Numerical Simulation of Nose Bluntness Effects on Hypersonic Boundary Layer Receptivity to Freestream Disturbances

Xiaolin Zhong[1] and Jia Lei[2]
University of California, Los Angeles, California 90095

Abstract

For hypersonic boundary layers over blunt cones, laminar-turbulent transition location moves down stream with increasing nose radii when they are relatively small. The transition reversal phenomenon refers to the experimental observation that the downward-moving trend reverses itself when the radii are larger than a certain critical value. Currently, there is no satisfactory explanation for the reversal. All previous linear stability theory (LST) and numerical simulation studies have not shown a reversal of instability or transition. The previous studies, however, have not been done on the actual experimental flow conditions which had shown transition reversal. The two most extensive experimental results on transition reversal are those reported by Stetson for Mach 5.5 flow over an 8 degree half-angle blunt cone and by Softley for Mach 10 flow over a 5 degree half-angle blunt cone. The objective of this paper is to conduct numerical simulation studies of the nose bluntness effects on freestream receptivity for Stetson's Mach 5.5 flow. Three test cases of both small and large nose radii are used to study the nose bluntness effects on the receptivity of boundary layers to freestream acoustic waves. The unsteady results are also compared with those of LST. The receptivity results of the current study do not show any reversal of instability due to increasing nose bluntness. In addition, the numerical-simulation and LST results show that the wave structures of different frequencies and different nose bluntness can be approximately scaled by the dimensionless frequency ω. Because relevant frequencies shift lower as nose radii increase, the same critical value of ω for second mode instability for different nose bluntness results in a downstream movement of instability location.

1 Introduction

The accurate prediction of laminar-turbulent transition in hypersonic boundary layers is a critical part of the aerodynamic heating analyses on hypersonic vehicles. Since 1950s, extensive wind-tunnel and flight-test experiments on boundary layer transition and a number of stability experiments have been conducted for hypersonic flows over circular cones [1, 2]. Schneider [1, 2] did an extensive review of the existing literature on these experiments for both flight test and wind tunnel experiments. Though many of these experiments did not measure transition mechanisms and were carried out in noisy wind tunnels, the experimental studies have led to better understanding of the effects on transition of many parameters, including nose bluntness, Mach number, freestream noise, surface and stagnation temperatures, freestream unit Reynolds numbers, cone half angles, angles of attack, and surface roughness, etc. Nevertheless, so far, the effects of many of these parameters on transition are still not well understood.

One of the unexplained phenomena is the transition reversal phenomenon as the nose bluntness of the cones increase [3, 4]. The transition reversal phenomenon refers to the experimental observation that the transition location

[1]Professor, Mechanical and Aerospace Engineering Department, AIAA Associate Fellow, Xiaolin@seas.ucla.edu.
[2]Graduate Student, Mechanical and Aerospace Engineering Department, AIAA student member, jxlei@ucla.edu.

moves downstream when the nose radius is increased. This trend is, however, reversed itself when the nose radius is larger than a certain critical value. Increasing nose radius after that will lead to a forward movement of the transition location. The downstream movement of the transition location at small radii can be explained by the reduction of local Reynolds numbers owing to the entropy layer created by the nose bluntness. However, there is still no satisfactory explanation for the cause of transition reversal at large nose bluntness. There is also a possibility that the surface roughness and freestream noise in wind tunnel play a role in the reversal.

Most of the previous theoretical and computational studies of the transition reversal have been on the Stetson *et al.'s* [5, 6] stability experiments on an axisymmetric blunt cone in a Mach 7.99 freestream. The half angle of the cone was 7°, the nose radii were 1.5 inches and larger, and the freestream Reynolds number based on the nose radius was 33,449. The Reynolds number based on the total length of the cone was about 9 millions. Detailed fluctuation spectra of the disturbance waves developing along the body surface were measured in the experiments. It was found that the disturbances in the boundary layer were dominated by the second mode instability. Significant super harmonic components of the second modes were observed after the second mode became dominant. Compared with similar hypersonic flow over a sharp cone, the second mode instability of the blunt cone appeared in much further downstream locations. This indicates a stabilization of the boundary layer by slight nose bluntness.

The normal-mode linear stability characteristics of the boundary-layer flow over the same blunt cone as Stetson *et al.*'s experiments have been studied by a number of researchers [7-10]. Malik *et al.* [7] computed the neutral stability curve and compared the growth rates obtained by LST with the experimental results. The steady base flow solution was computed by using the parabolized Navier-Stokes equations. They found that the nose bluntness stabilizes the boundary layer. The growth rates predicted by the LST were compared with Stetson *et al.*'s experimental results at the surface location of $s = 175$ nose radii (0.667 m). The linear stability analyses predicted slightly lower frequency for the dominant second mode, but much higher amplification rates than the experimental results. Rosenboom et al. [11] did further study on the effect of nose bluntness on the linear stability of hypersonic flow over Stetson's blunt cone. In their studies, the cone geometry and freestream conditions were adapted to the Stetson's experiments. Three cases of blunt cones of different nose radii, which cover both ``small'' and ``large'' bluntness, were considered. The purpose was to investigate, by linear stability analysis, the transition reversal phenomenon observed in experiments at ``large'' bluntness [4, 12]. By a linear stability analysis, Rosenboom et al. confirmed a monotonic downstream movement of the second mode critical Reynolds number as nose radius increases. However, their linear stability analysis still cannot explain the transition reversal phenomena observed in experiments at ``large'' bluntness. In addition to LST studies, Kara et al. [13] did a similar DNS study on the effects of nose bluntness on stability of a Mach 6 boundary layer over a 5-degree straight cone. They found that the bluntness has a strong stabilizing effect. Husmeier and Fasel [14] investigated the bluntness effects on nonlinear breakdown. Again, they found only stabilization effects on nose bluntness.

Zhong et al. [15-17] have conducted numerical simulation of the stability and receptivity of Stetson's Mach 8 flow over blunt cones. In [16], the numerical results for the steady base flow were compared with the experimental results of Stetson et al. [5], and with the numerical results of Esfahanian [18]. In addition, a normal-mode linear stability analysis was used to identify the main components of boundary-layer disturbances generated by forcing freestream fast acoustic waves. It was found that neither the first mode nor the second mode instability waves are excited directly by freestream fast acoustic waves in the early region along the cone surface, although the Mack modes can be unstable there. Instead, the second mode is excited downstream of the second-mode Branch I neutral stability point. The delay of the second-mode excitation is a result of the fact that the hypersonic boundary-layer receptivity is governed by a two-step resonant interaction process: 1) resonant interactions between the forcing waves and a stable boundary-layer wave mode I near the leading edge region, and 2) resonant interactions between the induced stable mode I and the unstable second Mack mode downstream.

The current work is motivated by our previous numerical simulation study [17] of the effect of nose bluntness on hypersonic boundary layer receptivity over a blunt cone. In [17], we conducted a numerical study on the effects of nose bluntness on the receptivity to free-stream acoustic waves for hypersonic flow by comparing the results of three nose radii. The flow conditions duplicated the experiments of Stetson et al. [5] and investigated the effects of nose bluntness on receptivity. Three nose radii were chosen to be the same as those used in Rosenboom et al.'s stability analysis. They are 3.81 mm, 17.78mm, and 42.67mm. The first nose radius belonged to category of ``small'' nose bluntness, while the second and third cases fell into the region of ``large'' bluntness. By using the numerical

simulation, the initial receptivity process was computed accurately. The effects of bow shock interaction with forcing waves, the effects of the entropy layer and non-parallel boundary layer are also taken into account in the numerical simulation. A total of 15 frequencies are computed in the receptivity simulation for each case. It is found that, in those three test cases, the basic receptivity mechanism of hypersonic flow over the blunt cone with different nose radii is essentially the same. Specifically, the receptivity is a result of the resonant interactions between forcing waves and boundary-layer wave modes near the nose region, and the resonant interactions between different boundary-layer wave modes downstream. As the nose radius increases from ``small'' to ``large'', the results in [5] showed no reversal in the location of instability wave induced by the receptivity process. In other words, the location of initial excitation of the second instability mode always moved downstream as the nose bluntness was increased.

Therefore, currently, the small bluntness effects of transition delay can be explained by the reduction of local Reynolds numbers. However, the mechanisms of transition reversal are not clear for the larger bluntness effects. The possible explanation for the experimental observation of transition reversal can be the instability of entropy layers, the surface roughness effects, wind tunnel noise in conventional noise tunnel, etc. So far, LST and computational studies have been done only on the test cases of Stetson's Mach 8 experiments [5]. All previous calculations have found no instability reversal at very large nose radii. On the other hand, Stetson's Mach 8 test model was not long enough to observe transition in his experiments. In other words, transition reversal phenomenon was not actually observed experimentally in Stetson's Mach 8 test cases. It is worthwhile to study, by both numerical simulation and LST, the mechanisms of transition reversal on the actual experimental conditions which have showed transition reversal.

Though the delay of transition by slight nose blunting has been found by many experiments since 1950s, the transition reversal at large nose bluntness has only been reported by a few researchers. Stetson et al. [3, 19] were the first ones to report concrete results on transition reversal. The only other reversal results were shown in Figure 3 of a paper by Ericsson [4], who cited an unpublished reported by Softley [20]. Therefore, the most extensive experimental results on transition reversal are those reported by Stetson especially the case of Mach 5.5 flow over sharp and blunt cones [3]. *Figure* 1 shows a schematic of Stetson's test models with ten nose radii: $\frac{1}{32}, \frac{1}{16}, \frac{3}{32}, \frac{1}{8}, \frac{5}{32}, \frac{6}{32}, \frac{7}{32}, \frac{1}{4}, \frac{1}{2}$, and $1\frac{1}{2} in$. The model was polished such that the general surface finish is approximately 10 μin and it can be considered to be smooth surface. Transition reversal was observed in these test models as shown in Figure 2, which shows the transitional Reynolds numbers vs. nose radius Reynolds numbers, which are based on freestream flow conditions. This figure is created by using Stetson's experimental results tabulated in Table 2 of [3]. The figure shows a clear transition reversal as Re_n increases, with the Re_n of 2×10^5 serving as the dividing line between "large" and "small" nose radii. This results are very similar to the results in [4] for freestream Mach number of 10 or higher.

So far, there has not been any LST or numerical simulation study on the Stetson's Mach 5.5 cases, which are one of the very few experimental test cases actually showing transition reversal. It will be valuable if these experiments can be systematically re-analyzed by modern numerical simulation and linear stability techniques to study the effects on transition by nose bluntness. Therefore, we have been conducting the LST [21] and numerical studies [22] of the cases of Stetson's Mach 5.5 experiments on the nose bluntness effects. Lei and Zhong [21] conducted a linear stability analysis on Stetson's Mach 5.5 experiments in which the reversal was observed. Three cones with nose radii of 0.156, 0.5, and 1.5 inches, covering both the "small" and "large" bluntness regions, were used to study the effect of nose bluntness on stability and transition. It was found that, if only the second-mode instabilities are considered, the onset of instability is always delayed as the nose bluntness increases. The LST calculations show no reversal on the growth of the second-mode instability. Zhong [22] did a numerical simulation study has on the mean flow and unsteady Mach 5.5 hypersonic flow over a blunt cone due to surface blow and suction. The flow conditions were the same as those of Stetson's 1967 wind-tunnel experiments for Mach 5.5 flows with same three cases of nose radii. The simulation results showed that the increase of nose bluntness leads to the substantial decrease in local Reynolds numbers along the edge of the boundary layers. The decrease of local Reynolds numbers is the main reason of transition delay by nose blunting in the small nose bluntness region. Only some preliminary results were reported for unsteady flow of boundary layer instability induced by surface blow and suction. Therefore, the objective of this paper is to conduct numerical simulation studies of the nose bluntness effects on freestream

receptivity for Stetson's Mach 5.5 flow. The same three test cases of both small and large nose radii are used to study the nose bluntness effects on the receptivity of boundary layers to freestream acoustic waves. The unsteady results are compared with those of LST obtained by Lei and Zhong [21].

We have developed a fifth-order shock-fitting code to compute the Navier-Stokes equations for such flows [23, 24]. The code has been used to study the study and unsteady hypersonic flow over a 7 degree blunt cone of Stetson's 1984 experiments [16, 17]. The use of high-order shock fitting schemes makes it possible to obtain highly steady and unsteady accurate solution of hypersonic flow over the cones with entropy layer effects. The steady mean flows can be used as a starting point for both the linear stability calculations of the same flow and the numerical simulation of freestream receptivity and stability of the boundary layers. By using the numerical simulation of the shock-fitting approach, the initial receptivity process can be computed accurately in the current study. The effects of bow shock interaction with forcing waves, the effects of the entropy layer and non-parallel boundary layer are also taken into account in the numerical simulation. Since the mean flow results have been reported by Zhong [22], they are not repeated in this paper.

2 Governing Equations and Numerical Methods

The governing equations for both steady and unsteady flow computations are briefly presented in this section. Details of the governing equations and numerical methods for two and three-dimensional flows have been described in previous papers[23, 25, 26]. The governing equations are the unsteady three-dimensional Navier-Stokes equations written in the following conservation-law form:

$$\frac{\partial U^*}{\partial t^*} + \frac{\partial F_j^*}{\partial x_j^*} + \frac{\partial F_{vj}^*}{\partial x_j^*} = 0 \tag{1}$$

where $U^* = (\rho^*, \rho^* u_1^*, \rho^* u_2^*, \rho^* u_3^*, e^*)$, and superscript "*" represents dimensional variables. The Cartesian coordinates, (x^*, y^*, z^*), are represented by (x_1^*, x_2^*, x_3^*) in the tensor notation. In the current simulation of three-dimensional flow over a blunt cone, x^* axis is along the center line of the axisymmetric cone pointing downstream. The origin of the Cartesian coordinate system is located at the center of the spherical nose cone.

For all results presented in this paper, unless specified otherwise, we nondimensionalize the flow velocities by the freestream velocity u_∞^*, length scales by the nose radius r_n^*, density by ρ_∞^*, pressure by p_∞^*, temperature by T_∞^*, time by r_n^* / u_∞^*, etc. The dimensionless flow variables are denoted by the same dimensional notation but without the superscript "*".

A 3-D fifth-order shock-fitting method of Zhong [23] is used to compute the flow field bounded by the bow shock and wall surface. In the discretization of the Navier-Stokes equations, spatial derivatives in the streamwise (s) and wall-normal (y_n) directions are modeled by a fifth-order finite difference schemes. The flow variables behind the shock are determined by the Rankine-Hugoniot relations across the shock and a characteristic compatibility equation from behind the shock. The details of the shock fitting formulas and numerical methods can be found in [23].

3 Flow Conditions

The flow conditions for the test case studied in this paper are the same as those in Stetson's experiments on air flow over a blunt cone in a Mach 5.5 freestream [3]. For the case of zero angle of attack, Stetson tested ten blunt cones of different nose radii ranging from 1/32 in to 1.5 in (see *Figure 1*). A range of different freestream unit Reynolds numbers were used to test these cones, from $1.6 \times 10^6 / ft$ to $18 \times 10^6 / ft$. In this paper, only three cases

of different nose radii and a constant unit Reynolds number are used in the numerical simulation. The nose radii of the three cases are:

$$\begin{aligned} &\text{Case 1: } r_n = 0.15625\ in = 3.969\ mm \\ &\text{Case 2: } r_n = 0.5\ in = 12.7\ mm \\ &\text{Case 3: } r_n = 1.5\ in = 38.1\ mm \end{aligned} \tag{2}$$

All other flow conditions are the same for these three cases. The specific flow conditions are:

- $M_\infty = 5.468$
- $P_\infty^* = 7756.56\,Pa$, $T_\infty^* = 174.46K$
- Wall temperature: $T_w = 296K$
- $\gamma = 1.4$, $\Pr = 0.72$, $R^* = 286.94Nm/kgK$
- Freestream unit Reynolds number: $\mathrm{Re}_\infty^* = 18.9714 \times 10^6 m^{-1}$
- Blunt cone half angle: $\theta = 8^\circ$, the freestream flow has a zero angle of attack
- Parameters in Sutherland's viscosity law: $T_r^* = 288K$, $T_s^* = 110.33K$,
  $\mu_r^* = 0.17894 \times 10^{-4} kg/ms$

where p_∞^* and T_∞^* are freestream pressure and temperature respectively. The body surface boundary condition is a non-slip condition for velocity and isothermal wall condition for temperature. In this particular study, both the steady base flow and unsteady flows are axisymmetric. The simulation is carried out by using 241 grid points between the cone surface and the shock (in the wall-normal direction). The simulation is carried out using many zones in the streamwise direction with about 20 grid point resolving one period of boundary layer wave modes.

As stated earlier in this paper, the origin of the Cartesian coordinate system, (x, y, z) , is located at the center of the nose of the spherical cone, where the x coordinate points from left to the right along the center line of the axisymmetric cone. In addition to x , a natural coordinate s is also used in this paper and in [3] to measure the dimensionless curve length of a surface location starting from the stagnation point. The nondimensional s and x , which are normalized by the nose radius r_n , are related to each other by the following relation:

$$x = \begin{cases} -\cos(s) & (s \le 0.5\pi - \theta) \\ (s + \theta - \pi/2)\cos\theta - \sin\theta & (s > 0.5\pi - \theta) \end{cases} \tag{3}$$

where θ is the half angle of the cone. In the current test case, $\theta = 8^\circ$.

4 Nose Bluntness Effects on Steady Base Flow

The steady base flow solution of the three test cases of different nose bluntness stated in (2) has been obtained by using a fifth-order shock fitting scheme. The steady results have been presented in [22]. The mean flow solutions are also used for a concurrent linear stability analysis in [21].

Figure 3 shows the Mach number contours for the three cases of steady base flow solution. The bow shock is obtained in the shock fitting simulation as the outer computational boundary of the contours. In all figures, unless marked with the dimensional units in the variables, the variables are dimensionless. The current figures show strong effects of the entropy layer near the nose region in case 3 of the largest nose radius. The boundary layer of case 3 is much thicker than that of case 1 for a sharper cone. Since the wave length of a boundary layer instability wave mode

is roughly twice the boundary layer thickness, the wave length of instability waves becomes longer as the nose bluntness increases. Meanwhile, the frequency of the unstable wave modes decreases.

It has been argued by many authors [3] that the cause of transition delay by slight nose bluntness is a result of the reduction of local Reynolds number at the edge of the boundary layer as the bluntness increases. For hypersonic flow over a blunt nose, the entropy layer behind the bow shock results in lower Mach numbers and local Reynolds numbers. If the local Reynolds number at transition remains a constant, the reduction of local Reynolds numbers leads to the downstream shift of the transition location. Since flow properties undergo substantial changes passing through the bow shock, the local unit Reynolds numbers were evaluated in [22] for the flow fields behind the bow shocks. It was shown that the cases of larger nose radii have thicker boundary layers and much lower local Reynolds numbers along the edge of the boundary layers.

5 Nose Bluntness Effects Analyzed by Linear Stability Theory

The linear stability theory (LST) was used by the authors in [21] to study the nose bluntness effects on the unstable wave modes for the three test cases considered in this paper. To apply the LST, the disturbance amplitudes are assumed to be small so that they do not interact non-linearly with each other. The normal mode of a disturbance variable is assumed to have the following form:

$$q' = \hat{q}(y_n)e^{i(-\omega t+\alpha s)} \tag{4}$$

where q' can be any dimensionless flow variable such as velocity, temperature, density and pressure, all of which are normalized by the freestream quantities. In the equation above, $\hat{q}$ is the mode structure representing the complex amplitude of the disturbances. In the spatial stability theory, ω, the dimensionless angular frequency of a normal disturbance mode, is set to be a real number, while $\alpha = \alpha_r + i\alpha_i$ is the stream-wise complex wave number non-dimensionalized by L^*. The imaginary part of wave number represents the spatial growth rate of a specific disturbance mode. When α_i is negative, the disturbance becomes unstable. The real part of the wave number α_r indicates the spatial wave number. An important quantity that can be extracted from α_r is the wave speed, which is defined as

$$a = \frac{\omega}{\alpha_r} = \frac{FR}{\alpha_r} \tag{5}$$

In the above equation, the dimensionless wave speed, a, is normalized by the free-stream velocity. The dimensionless frequency, ω, is defined as,

$$\omega = RF = \frac{\omega^* L^*}{u_\infty^*} \tag{6}$$

F is the dimensionless frequency that is related to the dimensional angular frequency by,

$$F = \frac{\omega^* \upsilon_\infty^*}{u_\infty^{*2}} \tag{7}$$

R is local Reynolds number based on the length scale of boundary layer thickness and s^* is the curvilinear coordinate along the cone surface as measured from the nose:

$$R = \frac{\rho_\infty^* u_\infty^* L^*}{\mu_\infty^*} \tag{8}$$

$$L^* = \sqrt{\frac{\mu_\infty^* s^*}{\rho_\infty^* U_\infty^*}} \tag{9}$$

Figure 4 shows the second-mode neutral stability curves for the three cases of different nose radii. As shown by Lei and Zhong [21], the second mode shown in this figure is in fact mode F when in becomes unstable. The neutral curve of Case 3 of 1.5 inch nose radius looks less smooth compared to those of the other two cases. This is a result of the fact that less data points in frequency domain are considered for this particular case. However, the general shape will not change much with more points added. In this figure, it is observed that the unstable second-mode spectrum falls into very different frequency ranges for cones of different nose bluntness. The frequencies of unstable second modes decrease for cones with larger nose radii. For the same cone at different surface locations, the unstable frequencies also gradually reduce when the waves propagate toward downstream locations. Overall, as the nose bluntness increases, the onset location of second-mode instabilities always moves downstream. As shown in the figure, no reversal is found on the LST result onset of instability locations.

For a supersonic boundary layer over a flat plate, Ma and Zhong [27] pointed out that the wave speeds (or phase velocities) and growth rates can be scaled by dimensionless frequency ω define by Eq. (6). In other words, the Brach I neutral stability location, as well as the synchronization location between mode F and mode S, approximately appear at the same ω, independent of frequency and location of the waves. On the other hand, the flow fields are more complex for the current hypersonic flow over blunt cones, where there is an interaction between the entropy layer and boundary layer. Such interaction does not exist in the flow field studied by Ma and Zhong [27]. Therefore, it is not clear if the same conclusion can be drawn for the current test cases.

The second-mode dimensional growth rates are plotted as a function of ω in *Figure 5* for the current three cases of hypersonic flow over blunt cones with different nose radii. Some common characteristics are observed in all these cases. First, the disturbances at higher frequencies become unstable at locations closer to the nose. Second, as the frequency decreases, the maximum second-mode growth rate becomes higher. Some trends are also found among these three cases. As the nose bluntness increases, the onset of the second-mode instability moves downstream in terms of dimensional coordinate s^*. The range of unstable mode frequency shifts to the lower end and becomes narrower as the nose becomes blunter. The frequency ranges shifting to lower value can be explained by the increase of boundary layer thickness due to blunting the nose, which causes the wave lengths of unstable modes to become longer. The growth rates for the blunter cone are substantially lower than those of the sharper cone. Also, for the blunter case, the instability of a fixed frequency tends to grow for a longer distance to compensate the lower growth rate it has. On the other hand, this figure shows that the region of mode F instability covers roughly the same interval of ω. For example, the peak growth rates for all three cases occur roughly at $\omega = 0.5$, even though the frequency ranges are very different for different nose radii.

The wave speeds and growth rates figures for a fixed frequency share many similarities with those at a fixed location with varying frequency. *Figure 6* shows the profiles of wave speeds for both mode F and mode S as functions of dimensionless frequency ω at a fixed surface location for the three cases of different nose radii. It was found in [21] that the unstable second mode is excited from the mode F. The mode F is defined as a discrete normal mode coming out of fast acoustic wave that has an initial non-dimensional wave speed of 1+1/*M*. Traditionally, *M* is the Mach number at the edge of boundary layer. Since the Mach number along the edge of boundary layer changes constantly for hypersonic flow over a blunt cone, the freestream Mach number is used to keep that wave speed constant as shown in this figure. Similarly, the slow acoustic wave has a non-dimensional wave speed of 1-1/*M*. In this case, both mode F and mode S are plotted to demonstrate a phenomenon called synchronization. Synchronization is a resonance between two normal modes of identical frequency when they have the same wave speed and frequency. The synchronization process provides a channel for energy exchange between two normal modes, which allows transfer of energy from stable mode to unstable mode. While other studies [16, 27] typically show mode S as the unstable second mode, our current cases show mode F becoming the unstable second mode. This switch can be explained theoretically due to the relatively cool wall surface temperature in the simulation [28].

Figure 6 shows the synchronization point between the two modes appears approximately at the same ω around 0.22 for all three cases. Since the frequency is lower for the blunter cones, a constant ω leads to a downstream movement of the synchronization point, as well as the instability region of the instability waves due to nose blunting. In other words, because the synchronization location of Case 3 occurs at the same ω but lower frequencies, larger surface length s^* is needed to reach the same value of ω.

6 Nose Bluntness Effects on Receptivity to Freestream Acoustic Waves

As discussed in Section 1, the main objective of this paper is to study the nose bluntness effects reported in the Stetson's experiments [3] (*Figure 2*). In this section, we present the results of the simulation study of receptivity to frestream acoustic disturbances for the three blunt cones with different nose bluntness. Various aspects of the linear stability of the flow can be studied by numerical simulation of receptivity of the boundary layer to various disturbances. Examples of the external disturbances include freestream perturbations, surface roughness, surface blow and suction, surface vibrations, etc. The forcing disturbances can be both 2-D and 3-D disturbances. In this paper, we will present the results of receptivity to freestream 2-D acoustic waves for the three cases of different nose radii.

In the current numerical simulation, the instability waves in the boundary layer are induced by imposing weak acoustic waves in freestream of the steady mean flow solution. Even though the nonlinear Navier-Stokes equations are used in the simulation, the amplitudes of the forcing waves are chosen to be weak enough so that the disturbances excited in the boundary layer are in the linear regime. In doing so, the results obtained from the simulation can be directly compared with those computed by the LST. In the unsteady flow simulation, we introduce, in the freestream, acoustic disturbances of a mixture of 15 frequencies. The subsequent shock interaction, receptivity and development of the instability waves in the boundary layer are computed by the numerical simulation. The specific frequencies of the forcing acoustic waves introduced in the freestream are

$$f_n^* = n f_1^* \qquad (n = 1, 2, \cdots, N) \tag{10}$$

where the range of frequencies for each nose radius is determined by the corresponding LST analysis so that the most unstable waves are included in the simulation. The specific frequencies used for the three cases are

- Case 1: $r_n = 0.156$ *in*, $f_1^* = 52.5509$ *kHz*, $\cdots$, $f_{15}^* = 788.26$ *kHz*
- Case 2: $r_n = 0.5$ *in*, $f_1^* = 32.1144$ *kHz*, $\cdots$, $f_{15}^* = 481.72$ *kHz*
- Case 3: $r_n = 1.5$ *in*, $f_1^* = 20.0$ *kHz*, $\cdots$, $f_{15}^* = 300.0$ *kHz*

All 15 frequencies for each case are multiples of f_1^* given by Eq. (10).

Since the purpose of the current study is to study the linear stability of the boundary layer, the overall free-stream wave amplitude used in the simulation is $\varepsilon = 5 \times 10^{-4}$, which is sufficiently small so that the receptivity process falls in the linear regime. Consequently, the wave components of the 15 frequencies are independent, and they can be decomposed one from another by a temporal Fourier analysis. Since the wave components of different frequencies are linearly independent, the relative wave amplitudes among different frequencies in the free stream are set to be the same, while the phase angles ϕ_n of the forcing waves at frequency ω_n are chosen randomly.

The unsteady calculations are carried out until the solutions reach a periodic state in time. Temporal Fourier analysis is then carried out on the local perturbations of unsteady flow variables. For example, a Fourier transform for the perturbation field of an arbitrary flow variable leads to

$$q'(x, y, t) = \mathrm{Re}\left(\sum_{n=0}^{N} | q_n(x, y) | \; e^{i[-2\pi f_n t + \phi_n(x,y)]} \right) \tag{11}$$

where f_n is the frequency and $q'(x, y, t)$ represents an arbitrary perturbation variable. The Fourier transformed variables, $|q_n(x, y)|$ and $\phi_n(x, y)$, are spatially varying real variables representing the local perturbation amplitudes and phase angles at the wave frequency of f_n. For perturbations on the body surface, the growth rates and wave speeds of the perturbations corresponding to f_n can be computed according to the following formulas:

$$\alpha_i = \frac{d\,|q_n|}{ds}\frac{1}{|q_n|}$$
$$a = \frac{\omega_n}{\alpha_r} = \frac{2\pi f_n}{d\phi_n / ds} \tag{12}$$

where $|q_n|$ is the amplitude of surface pressure perturbations obtained by a temporal Fourier analysis of the instantaneous pressure.

If flow perturbations obtained by the receptivity simulation are dominated by a single wave mode, such as the unstable mode F in the current cases, the parameters computed by Eq. (12) are the growth rates and wave speeds of this mode. In this case, profiles of α_i and a as functions of natural coordinate s are smooth lines with no oscillations. On the other hand, if the simulation results contain a modulation of multiple wave modes in a local region of the boundary layer, α_i and a computed by Eq. (12) do not represent the growth rates and wave speed of a single wave mode. Instead, these two parameters represent a modulation of two or more wave modes. As a result, the profiles of α_i and a along the surface direction will be oscillatory functions of s. In this case, further decomposition of different wave components is required in order to obtain the growth rates and wave speeds of the individual wave modes.

Case 1: Nose Radius=0.156 in.

The results of receptivity simulation for case 1 of sharpest cone are considered. The freestream Reynolds number based on the nose radius is 7.5212×10^4, which falls into the small nose radius regime in *Figure 2*.

Figure 7 shows the amplitude profiles of surface pressure perturbations, i.e., $|p_n(s)|$ computed by Eq. (12), along the dimensional length of the cone surface. Each line represents the response of the boundary layer to freestream forcing waves at one of the 15 frequencies ranging from 52.5 kHz for n=1 to 788.3 kHz for n=15. Dimensional surface length s^* is used in the figure so that the results of the three cases can be compared. This figure shows that the receptivity process leads to complex wave structures in the boundary layer. For perturbations of a fixed frequency, the disturbance wave structures change dramatically as they propagate downstream. The wave structures for the receptivity of a Mach 8 flow over a cone were analyzed by Zhong and Ma [29]. The basic wave structures of the current case are to those studied in [29], with the exception that mode F is unstable in the current case as compared to unstable mode S in the Mach 8 flow studied by Zhong and Ma.

Figure 7 shows similar amplitude development for all 15 frequencies. Specifically, there is strong wave modulation in the early region immediate behind the nose cone. The length of this initial wave region is very short for the highest frequency of n=15. As the frequency decreases, this initial transient region spans longer and longer length downstream. The initial modulation region is followed by a region of a single mode F induced by external forcing. Further downstream, the wave amplitude grows exponentially due to mode F, or the second mode, instability. For example, for the frequency of n=13 ($f_{13}^* = 683.2\ kHz$), *Figure 7* shows that for the initial transient region of $s^* < 0.24\ m$, where the wave amplitudes show strong wave modulation due to initial interaction of forcing waves with the boundary layer. As the wave propagates past this initial region, the amplitude for this frequency shows a clean line with little modulation. This is an indication that the unsteady solution consists of mostly a single mode F in the boundary layer. This second region for the frequency of f_{13}^* is $0.24\ m \le s^* < 0.5\ m$. In the second region, the wave amplitude grows along the surface as a result of resonant interaction between the external acoustic forcing waves and mode F. As the waves of f_{13}^* propagate further downstream of $s^* > 0.5\ m$, the wave amplitude experience exponential growth as shown by this figure. This third region is the region of second mode instability, which is consistent with the LST result of Lei and Zhong [21]. This

figure also shows that the growth of unstable mode F in the third region is mixed with external acoustic waves as demonstrated by a strong wave modulation in this region. The wave amplitude profiles of all other frequencies demonstrate similar characteristics of three regions of (1) initial transient modulation, (2) subsequent relative clean mode F development, and (3) eventual mode F instability. For a lower frequency, these three regions are stretched longer in the dimensional surface natural coordinate s^*. For the current case of 0.156 inch nose radius, the unstable waves excited by freestream forcing waves start approximately at the surface location of $s^* \approx 0.5\ m$ for higher frequencies of $f_{12}^* = 630.6\ kHz$ and $f_{13}^* = 683.2\ kHz$. For disturbances of lower frequencies, the computation domain is not long enough for the simulation results to reach mode F instability region.

Similar to the discussions on *Figure 5* and *Figure 6*, a more appropriate dimensionless parameter representing surface length for wave development inside the boundary layer is the dimensionless frequency ω. *Figure 8* shows the same amplitude profiles of surface pressure perturbations as a function of dimensionless frequency ω for the six of the 15 frequencies shown in *Figure 7*. It is interesting to note that the amplitudes induced by freestream acoustic waves of different frequencies approximately scaled to a single profile for $\omega < 0.5$. This shows that the mechanisms in the earlier region before the mode F instability are the same for different frequencies. The receptivity results agree with the LST results that ω is the appropriate scaling parameter for the wave fields.

Figure 9 shows wave-speed distributions of the pressure perturbations for two frequencies, n=12 and n=13. The profiles are plotted as a function of (a) dimensionless frequency ω and (b) dimensional surface length. The receptivity results on the left figure are also compared with the corresponding LST ones. The same plots of four lower frequencies are shown in *Figure 10*. As shown in the figures, there is a strong presence of forcing fast acoustic waves in the results. For the frequency of n=12, the left plot of *Figure 9* shows the mode F instability becomes dominant for $\omega > 0.5$, where the wave speeds for mode F predicted by LST go through the center of the distribution of the receptivity simulation results. This is a reasonable agreement considering the strong modulation by the external forcing waves. Again, the wave profiles of different frequencies are scaled very well by ω.

The modulation of acoustic forcing waves in the boundary layer can also be demonstrated by the contours of the disturbance fields. The wave patterns in the flow field can be represented by contours of the real part of the temperature perturbations, which can be computed by a temporal FFT analysis of the simulation results as shown in [29]. *Figure 11* and *Figure 12* show the contours of the real part of the temperature and pressure perturbations in a section of the computational flow field for the frequency of $f_{13}^* = 683.121\ kHz$. The upper boundary of the computational domain is the bow shock, while the lower one is the cone surface. The flow direction is from the left to the right. The wave fields contain strong external acoustic waves induced by the forcing waves introduced in the freestream over the shock wave. The enlarged plots for the region on the wall show the development of unstable mode F on the wall. The external fast acoustic waves, which have shorter wave length than that of the mode F, can be seen clearly on top of the wave filed inside the boundary layer. The wave fields in the small region near the wall for three other frequencies are shown in *Figure 13*, which shows different stage of mode F development at different frequencies. The effects of forcing waves in the receptivity process are very clearly shown in the figures.

Figure 14 compares the wave structures of the induced boundary-layer disturbances at $s^* = 0.586\ m$ with the eigenfunctions of mode F computed by the LST. The frequency is $f_{13}^* = 683.121\ kHz$. This location is in the mode F unstable region as shown by *Figure 7*. The receptivity flow field also contains strong acoustic forcing waves outside the boundary layer. Nevertheless, *Figure 14* shows a good agreement between the current receptivity simulation and mode F inside the boundary layer on the wall ($y_n^* < 0.003\ m$). As expected, the agreement away from the wall is not good as good because of the external forcing waves. Similarly, a good agreement between the receptivity results and LST mode F is also found for the lower frequency of $f_{12}^* = 630.610\ kHz$ as demonstrated in *Figure 15*. There is a good agreement in the pressure and temperature perturbations except for visible differences outside the boundary layer. The differences outside the boundary layer are caused by the fact that, in addition to the mode F waves, there are also forcing acoustic wave components in the induced flow field. The modulation of external forcing waves and the induced mode F in the boundary layer can be seen in *Figure 16* for

$f_{11}^* = 578.060\ kHz$ where the waves outside the boundary layer are very strong. *Figure 17* shows the profiles of two more frequencies on the wall.

To summarize the results of case 1, the induced mode F by the receptivity process begins to develop instability around $s^* \approx 0.5\ m$ for the current case of 0.156 inch in nose radius. In addition, the wave fields of different frequencies can be scaled very well by a single dimensionless frequency ω.

Case 2: Nose Radius=0.5 in.

The results of receptivity simulation for case 2 of intermediate nose bluntness are considered. The freestream Reynolds number based on the nose radius is 2.4068×10^5, which falls into the border between small and large nose radius regime in *Figure 2*.

Figure 18 to *Figure 20* show the amplitude distributions of surface pressure perturbations, i.e., $|p_n(s)|$ computed by Eq. (12), as functions of (a) the dimensionless frequency ω and (b) the dimensional length of the cone surface s^*. Again, each line represents the response of the boundary layer to freestream forcing waves at one of the 15 frequencies ranging from 32.1 kHz for n=1 to 481.7 kHz for n=15. The figures show similar receptivity results for the current case and case 1 of the sharper cone. Specifically the mode F instability starts approximately at $\omega \approx 0.5$. Because the dimensional frequency in this case is lower, Eq. (6) shows that the corresponding s^* will be larger for the current case. *Figure 18* shows that mode F will not be unstable until $s^* > 1.5\ m$, which is much larger than the location of 0.5 m for case 1. Therefore, nose blunting leads to downstream movement of the instability region for mode F. These three figures also show that when the amplitudes are plotted against ω, the amplitudes of different frequencies are much closer to a single line.

Figure 21 and *Figure 22* show the phase velocity distributions of pressure perturbations for different frequencies as a function of (a) dimensionless frequency ω and (b) dimensional surface length s^*. As shown in these figures, there is a strong presence of the forcing fast acoustic waves in the results. For the frequency of n=13, mode F instability becomes dominant for $\omega > 0.5,$ which is approximately the same ω as that for case 1 of the sharper cone. Again, the wave profiles of different frequencies are scaled better by ω for different frequencies and different nose radii.

To summarize the results of case 2, the induced mode F by the receptivity process begins to developed instability around $s^* \approx 1.5\ m$ for the current case of 0.5 inch in nose radius.

Case 3: Nose Radius=1.5 in.

The results of receptivity simulation for case 3 of largest nose bluntness are considered. The freestream Reynolds number based on the nose radius is 7.2204×10^5, which falls into the large nose radius regime in *Figure 2*. The experimental results show reversal of the transition location when the nose radius increase from 0.5 in. of case 2 to 1.5 in. for the current case.

Figure 23 to *Figure 25* show the amplitude distributions of surface pressure perturbations along the dimensional length of the cone surface. Each line represents the response of the boundary layer to freestream forcing waves at one of the 15 frequencies ranging from 20 kHz for n=1 to 300 kHz for n=15. Both dimensional surface length s^* and dimensionless frequency ω are used in the figures. In this case, the computational domain of 3.6 meters is not long to reach mode F instability region. Again, the mode F instability is expected to start approximately at $\omega \approx 0.5$, but the current computational domain ends at $\omega \approx 2.6$ for the highest frequency of n=15. The growth of wave amplitudes shown in these figures is not a result of exponential instability of mode F. Instead, it is due to a resonant interaction between stable mode F and the forcing fast acoustic waves. These three figures also show that when the

amplitudes are plotted against ω, the amplitudes of different frequencies are much closer to a single line. *Figure 26* shows the phase velocity distributions of pressure perturbations of different frequencies, as a function of dimensionless frequency ω for different frequencies. Again, the wave profiles of different frequencies are scaled very well by ω for different frequencies and different nose radii.

To summarize the results of case 3, the induced mode F by the receptivity results do not develop instability at the end of the computational domain of $s^* \approx 3.6\ m$ for the current case of 1.5 inch in nose radius. All three cases of increasing nose radii show the consistent downstream movement of the location of mode F instability. The receptivity results do not show any reversal in instability as the nose bluntness increases.

7 Conclusions

A numerical simulation study has been conducted on the mean flow and the receptivity of Mach 5.5 hypersonic flow over a blunt cone due to freestream fast acoustic waves. The flow conditions are the same as those of Stetson's 1967 wind-tunnel experiments for Mach 5.5 flow over a 8° half-angle blunt cone. These experiments are among the very few cases showing transition reversal due to nose bluntness. In this paper, three nose radii of 0.0156, 0.5, and 1.5 inches are used to study the mechanisms of the transition reversal. The simulation results show that the increase of nose bluntness leads to the substantial decrease in local Reynolds numbers along the edge of the boundary layers. The decrease of local Reynolds numbers is the main reason of transition delay by nose blunting in the small nose bluntness region. On the other hand, the cause of transition reversal in large nose bluntness regime is still not clear. We have finished three cases of receptivity for unsteady flow of boundary layer instability induced by freestream fast acoustic waves. All three cases of increasing nose radii show a consistent downstream movement of the location of mode F instability. The receptivity results do not show any reversal due to the increase of nose bluntness. The numerical and LST results show that the wave profiles can be scaled by ω for different frequencies and different nose radii. In other words, the second mode instability starts roughly $\omega \approx 0.5$ for the three cases of small and large nose radii. Because the frequency shifts lower as the nose radius increases, it can explain the downstream movement of the dimensional instability location s^* in order to maintain a constant ω for the second mode instability region.

Acknowledgments

This work was sponsored by AFOSR/NASA National Center of Hypersonic Research in Laminar-Turbulent transition. The views and conclusions contained herein are those of the authors and should not be interpreted as necessarily representing the official policies or endorsements either expressed or implied, of the Air Force Office of Scientific Research or U.S. Government.

References

1. Schneider, S.P., *Hypersonic Laminar-Turbulent Transition on Circular Cones and Scramjet Forebodies.* Progress in Aerospace Sciences, 2004. **40**: p. 1-50.
2. Schneider, S.P., *Flight Data for Boundary-Layer Transition at Hypersonic and Supersonic Speeds.* Journal of Spacecraft and Rockets, 1999. **36**(1): p. 8-20.
3. Stetson, K.F., Rushton, G. H., *Shock Tunnel Investigation of Boundary-Layer Transition at M = 5.5.* AIAA JOURNAL, 1967. **5**(5): p. 899-906.
4. Ericsson, L.E., *Effects of Nose Bluntness and Cone Angle on Slender Vehicle Transition.* AIAA Paper 87-1415, 1987.
5. Stetson, K.F., Thompson, E. R., Donaldson, J. C., and Siler, L. G., *Laminar Boundary Layer Stability Experiments on a Cone at Mach 8, Part 2: Blunt Cone.* AIAA paper 1984-0006, 1984.
6. Stetson, K.F., and Kimmel, R., *On the Breakdown of a Hypersonic Laminar Boundary Layer.* 1993. **AIAA Paper 93-0896**.
7. Malik, M.R., Spall, R. E., and Chang, C. L., *Effect of Nose Bluntness on Boundary Layer Stability and Transition.* AIAA Paper 1990-0112, 1990.
8. Herbert, T.a.E., V., *Stability of Hypersonic Flow over a Blunt Body.* AGARD CP, 1993. **514**: p. 28.

9. Kufner, E., Dallmann, U., and Stilla, J., *Instability of Hypersonic Flow Past Blunt Cones - Effects of Mean Flow Variations.* AIAA paper 1993-2983, 1993.
10. Kufner, E., and Dallmann, U. *Entropy and Boundary Layer Instabilityof Hypersonic Cone Flows - Effects of Mean Flow Variations*. in *IUTAM Symposium on Laminar-Turbulent Transition*. 1994. Sendai/Japan: Springer-Verlag, Berlin.
11. Rosenboom, I., Hein, S., and Dallmann, U., *Influence of Nose Bluntness on Boundary-Layer Instabilities in Hypersonic Cone Flows* AIAA Paper 99-3591, 1999.
12. Potter, J.L., and Whitfield, J. D. *Boundary-Layer Transition under Hypersonic Conditions*. in *Recent Developments in Boundary Layer Research, Part III*. 1965.
13. Kara, K., *Effects of Nose Bluntness on Stability of Hypersonic Boundary Layers over a Blunt Cone.* AIAA paper 2007-4492, 2007.
14. Husmeier, F., Fasel HF., *Numerical investigations of hypersonic boundary layer transition for circular cones*, in *AIAA CFD Conf., 18th*. 2007: Miami, FL.
15. Zhong, X., *Numerical Simulation and Experimental Comparison of Hypersonic Boundary Layer Instability over a Blunt Cone.* AIAA paper 2004-2244, 2004.
16. Zhong, X., and Ma, Y., *Boundary-layer receptivity of Mach 7.99 Flow over a blunt cone to free-stream acoustic waves.* Journal of Fluid Mechanics, 2005. **556**: p. 55-103.
17. Zhong, X., *Effect of Nose Bluntness on Hypersonic Boundary Layer Receptivity over a Blunt Cone.* AIAA paper 2005-5022, 2005.
18. Esfahanian, V., *Computation and stability analysis of laminar flow over a blunt cone in hypersonic flow*. 1991, The Ohio State University.
19. Stetson, K.F., *Nosetip Bluntness Effects on Cone Frustum Boundary Layer Transition in Hypersonic Flow.* AIAA paper 1983-1763, 1983.
20. Softley, E.J., *Transition of the Hypersonic Boundary Layer on a Cone: Part II - Experiments at Mach 10 and More on Blunt Cone Transition*, in *GE Space Science Lab, R68SD14*. 1968.
21. Lei, J., and Zhong, X., *Linear Stability Analysis of Nose Bluntness Effects on Hypersonic Boundary Layer Transition.* AIAA paper 2010-0898, 2010.
22. Zhong, X., *Numerical Simulation of Hypersonic Boundary Layer Receptivity and Stability on Blunt Circular Cones.* AIAA paper 2009-0940, 2009: p. 1-20.
23. Zhong, X., *High-Order Finite-Difference Schemes for Numerical Simulation of Hypersonic Boundary-Layer Transition.* Journal of Computational Physics, 1998. **144**: p. 662-709.
24. Lei, J., and Zhong, X., *Linear Stability study of Hypersonic Boundary Layer Transition on Blunt Circular Cones* AIAA Paper 2009-0939, 2009.
25. Zhong, X., *Leading-Edge Receptivity to Free Stream Disturbance Waves for Hypersonic Flow over a Parabola.* Journal of Fluid Mechanics, 2001. **441**: p. 315-367.
26. Zhong, X., *Additive Semi-Implicit Runge-Kutta Schemes for Computing High-Speed Nonequilibrium Reactive Flows.* Journal of Computational Physics, 1996. **128**: p. 19-31.
27. Ma, Y., and Zhong, X., *Receptivity of a Supersonic Boundary Layer over a Flat Plate. Part 1: Wave Structures and Interactions.* Journal of Fluid Mechanics, 2003. **488**: p. 31-78.
28. Fedorov, A., *Receptivity of a high-speed boundary layer to acoustic disturbances.* Journal of Fluid Mechanics, 2003. **491**: p. 101-129.
29. Zhong, X., and Ma, Y., *Boundary-layer receptivity of Mach 7.99 flow over a blunt cone to free-stream acoustic waves.* Journal of Fluid Mechanics, 2006. **556**: p. 55-103.

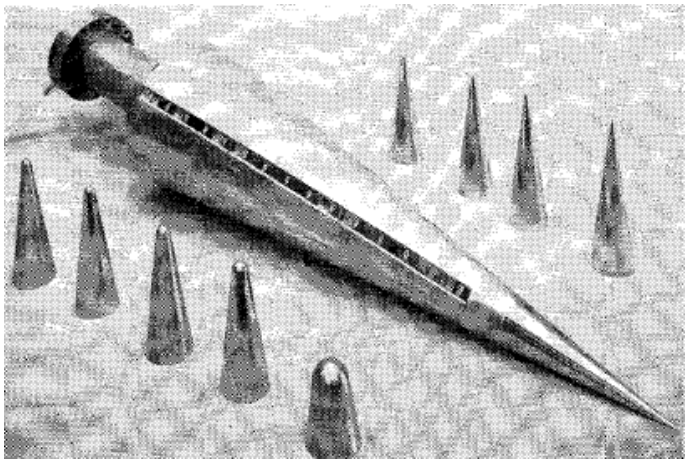

Figure 1. Sharp and blunt cone models with an 8 degree half angle used in Stetson's transition experiments in a Mach 5.5 shock tunnel [3].

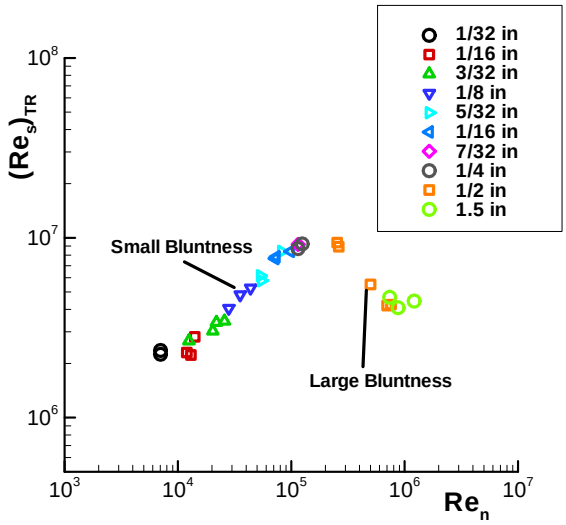

Figure 2. Transitional Reynolds numbers vs. nose radius Reynolds numbers, based on freestream flow conditions, for Stetson's Mach 5.5 experiments (from Table 2 of [3]). The legends specify the nose radii of the test cases.

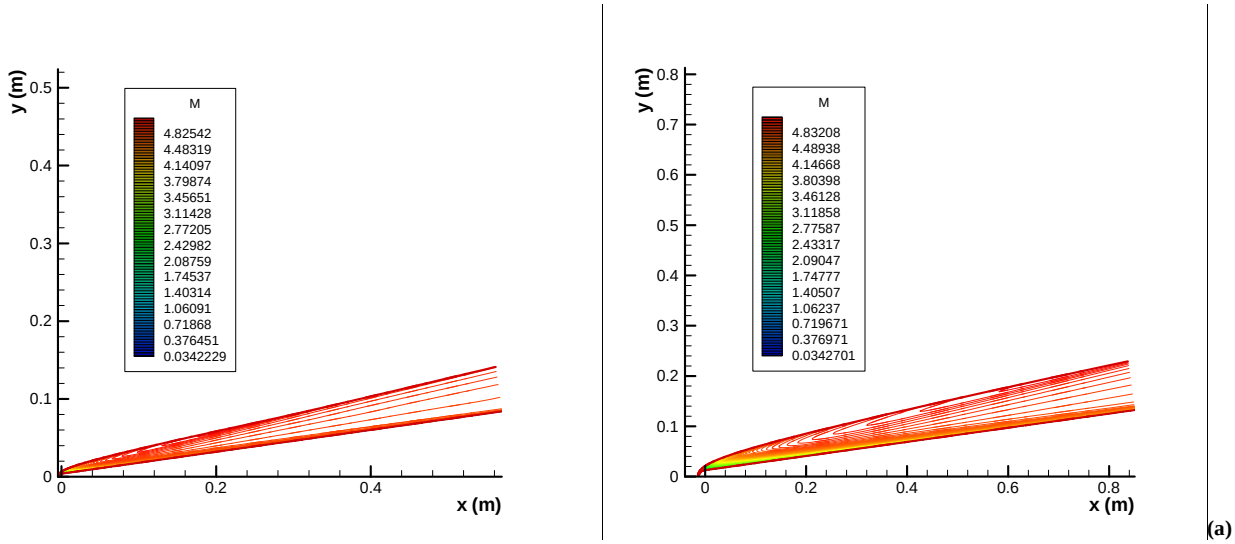

(Case 1: : $r_n = 0.156\ in.$**)** **(Case 2: :** $r_n = 0.5\ in.$**)**

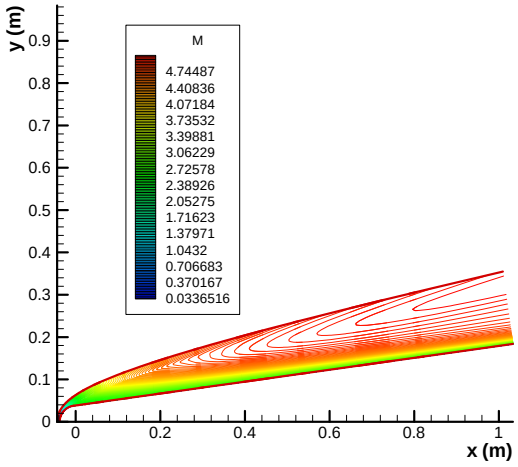

(Case 3: $r_n = 1.5\ in.$**)**

Figure 3. Steady Mach number contours of the three test cases of different nose radii.

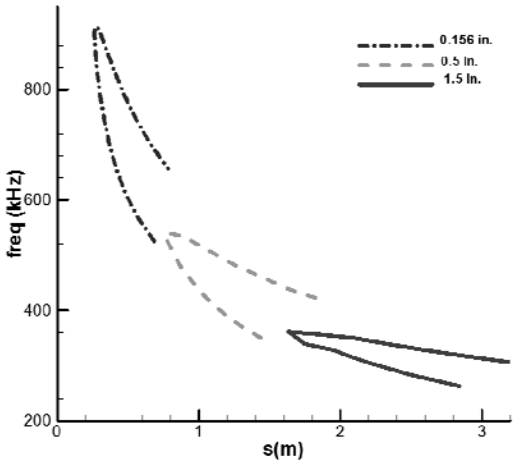

Figure 4. Second-mode (or mode F) neutral stability curve for the current blunt cones with three different nose radii.

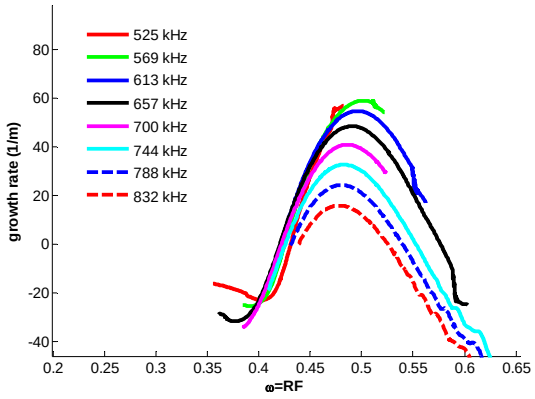

(*Case 1, nose radius =0.156 in.*)

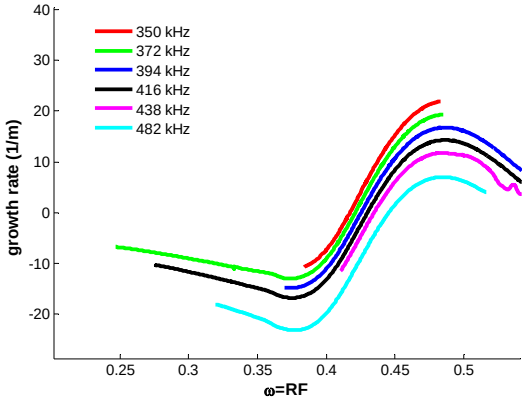

(Case 2, nose radius=0.5 in.)

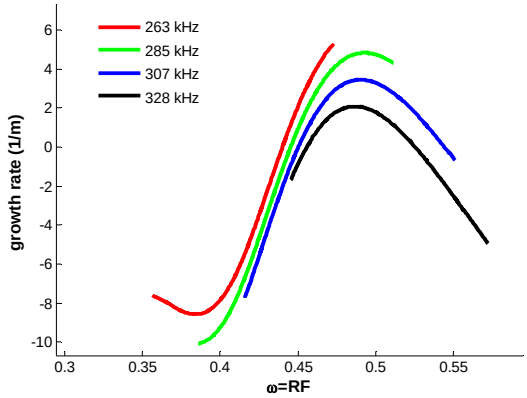

(*Case 3, nose radius=1.5 in.*)

Figure 5. Dimensional growth rates of mode F (the second mode) as a function of dimensionless frequency ω for the three cases of different nose radii.

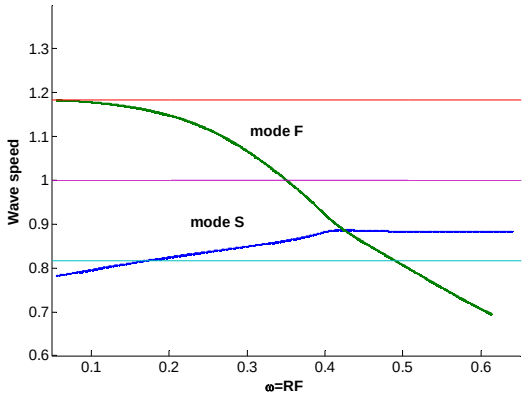

(*Case 1, 0.156 in, S*=0.41m*)

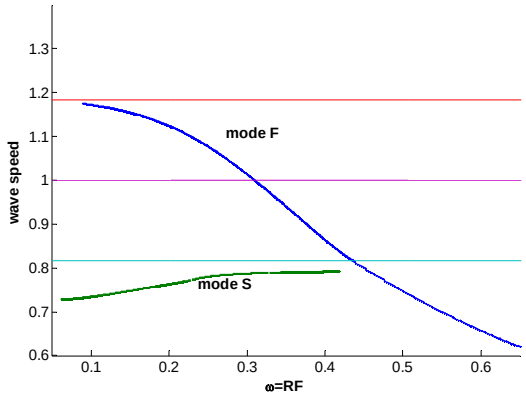

(*Case 2, 0.5 in, S*=1.01m*)

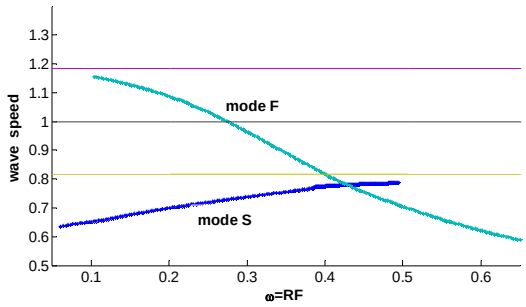

(*Case 3, 1.5 in, S*=1.95m*)

Figure 6. Distributions of wave speeds of mode F and mode S as functions of dimensionless frequencies at a fixed surface location for the three cases of different nose radii.

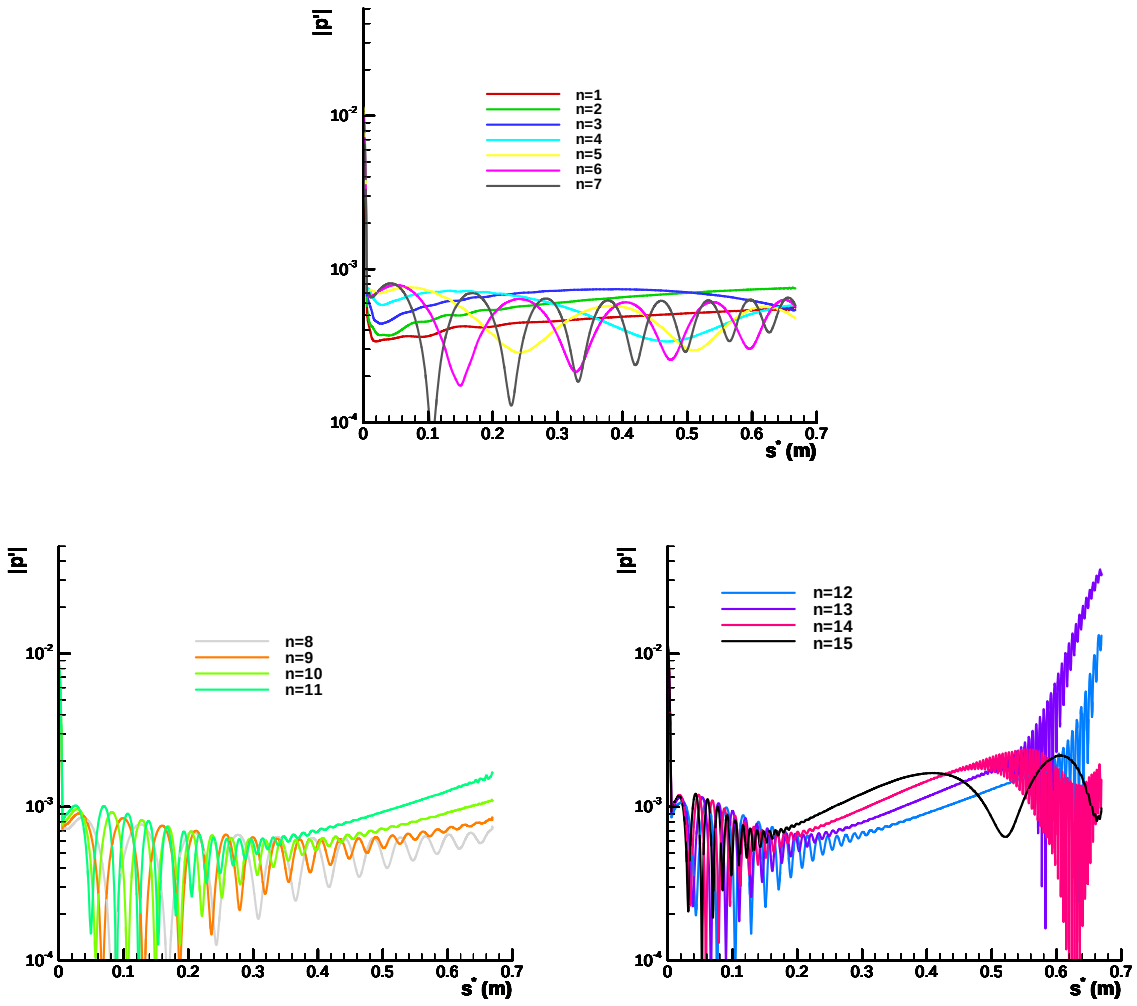

Figure 7. Amplitude profiles of surface pressure perturbations along the dimensional length of the cone surface. The lines represent 15 different frequencies of $f_n^* = nf_1^*$ ***, where*** $f_1^* = 52.55$ kHz ***and*** $n = 1,\ 2,\ \ldots,\ 15$ ***for Case 1 of nose radius of 0.156 in.***

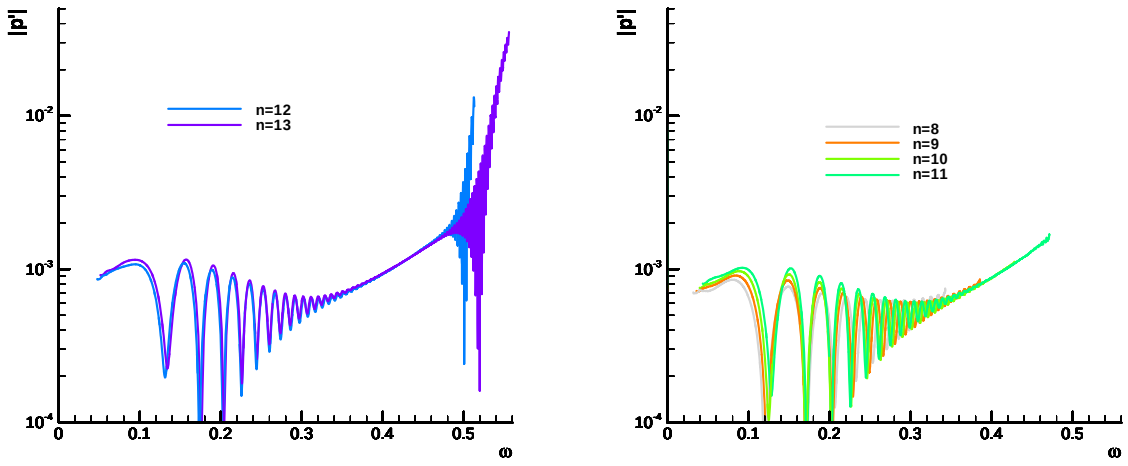

Figure 8. Amplitude distributions of surface pressure perturbations as a function of dimensionless frequency ω. The lines represent different frequencies of $f_n^* = nf_1^*$, where $f_1^* = 52.55$ kHz for Case 1 of nose radius of 0.156 in.

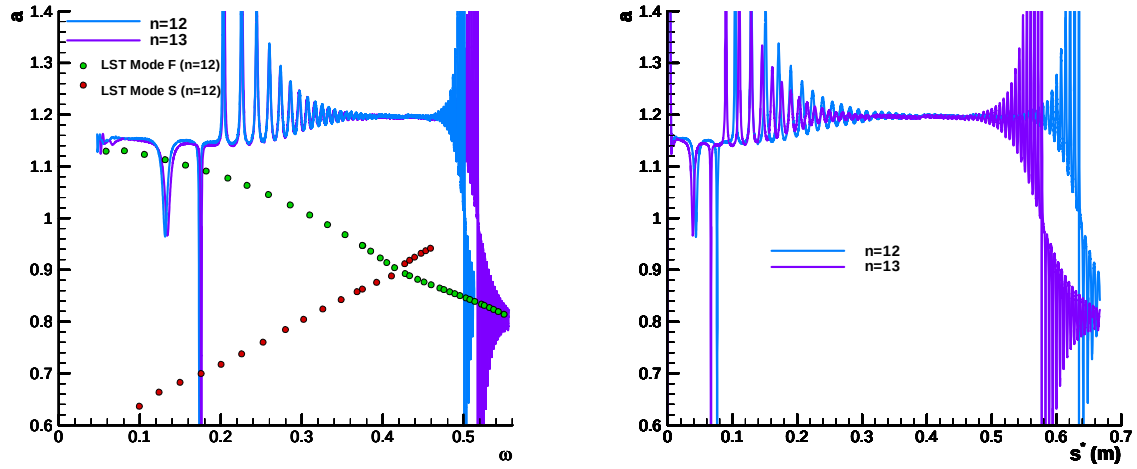

(a) **(b)**

Figure 9. Phase velocity distributions of pressure perturbations as a function of (a) dimensionless frequency ω and (b) dimensional surface length. The lines represent different frequencies of $f_n^* = nf_1^*$, where $f_1^* = 52.55$ kHz for Case 1 of nose radius of 0.156 in. The results on the left plot are compared with the corresponding LST ones.

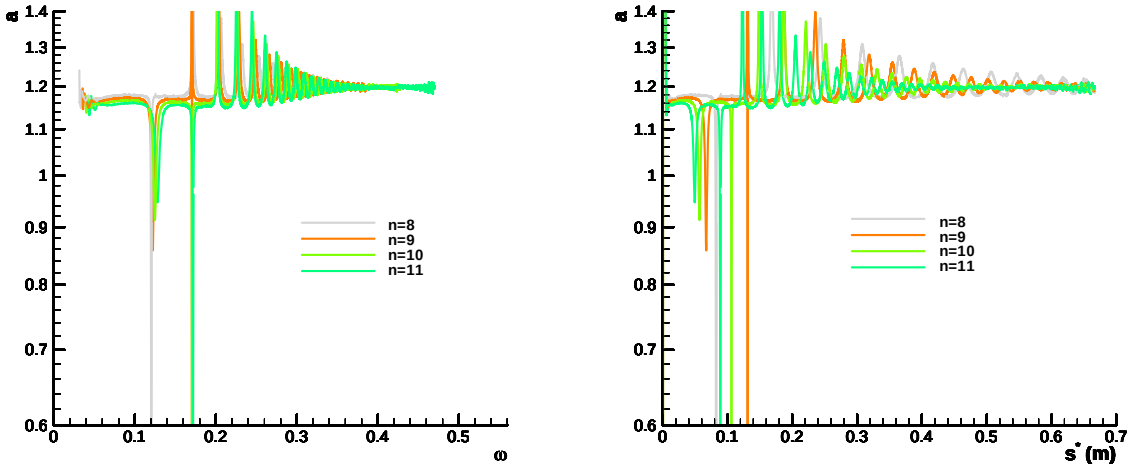

(a) **(b)**

Figure 10. Phase velocity distributions of pressure perturbations as a function of (a) dimensionless frequency ω and (b) dimensional surface length. The lines represent different frequencies of $f_n^* = nf_1^*$, where $f_1^* = 52.55$ kHz for Case 1 of nose radius of 0.156 in.

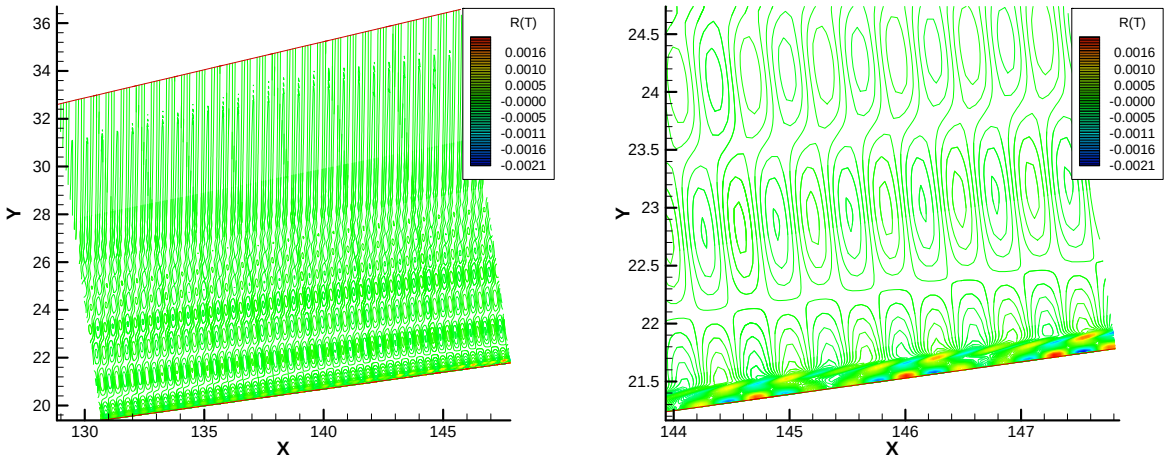

Figure 11. Contours of the real part of temperature perturbations for unsteady flow with $f_{13}^* = 683.121$ kHz for Case 1 of nose radius of 0.156 in. Left plot shows an enlarged view of a local region on the wall.

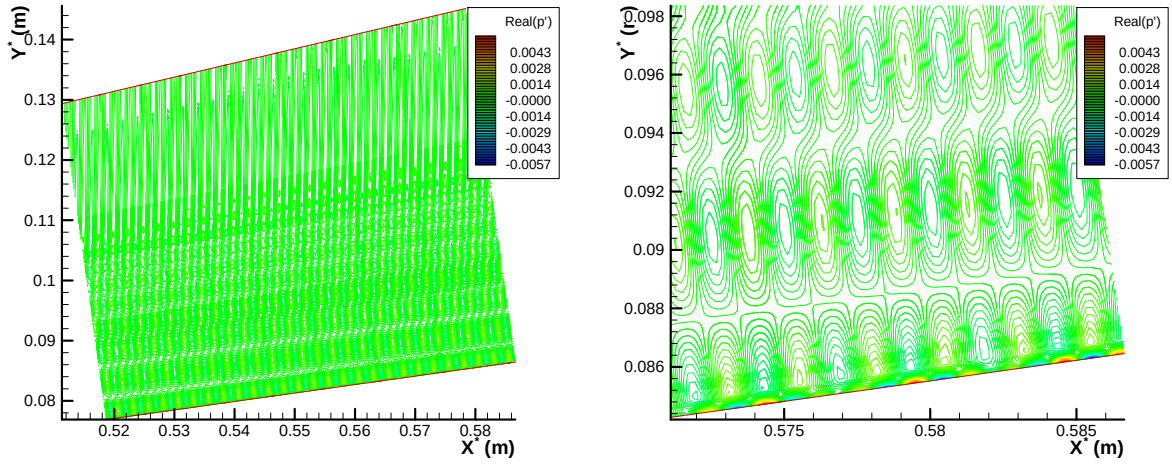

Figure 12. Contours of the real part of pressure perturbations for unsteady flow with $f_{13}^{*} = 683.121\ kHz$ ***for Case 1 of nose radius of 0.156 in. Left plot shows an enlarged view of a local region on the wall.***

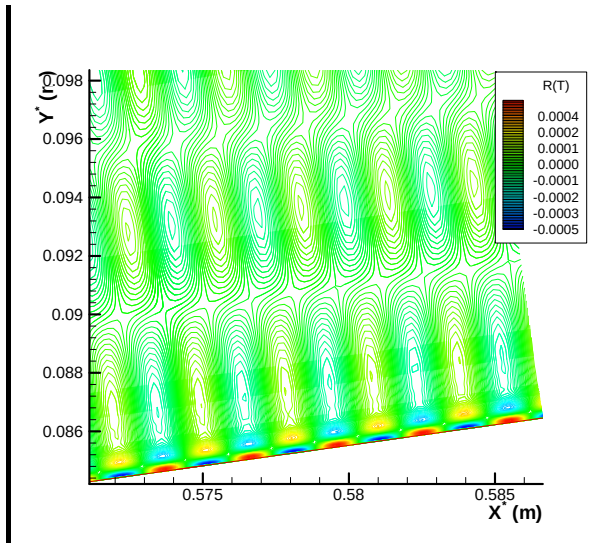

($f_{11}^{*} = 578.060\ kHz$)

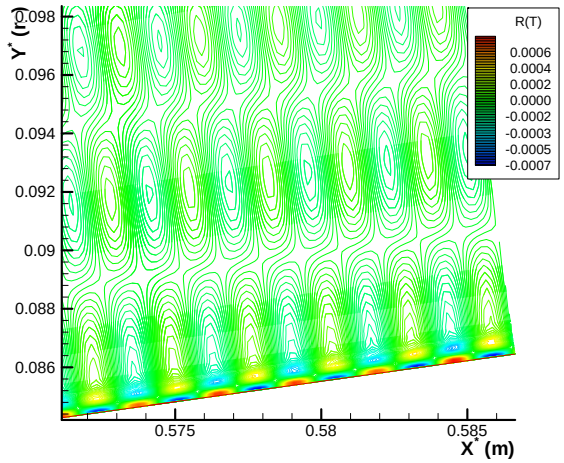

($f_{12}^{*} = 630.610\ kHz$)

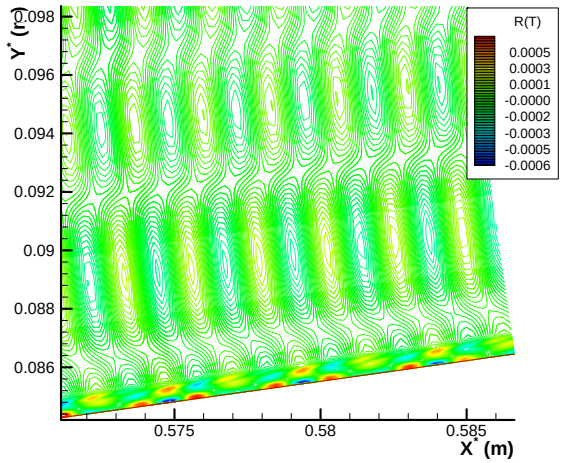

($f_{14}^{*} = 735.712\ kHz$)

Figure 13. Contours of the real part of temperature perturbations for unsteady flow with three frequencies for Case 1 of nose radius of 0.156 in. All plots show an enlarged view of a local region on the wall.

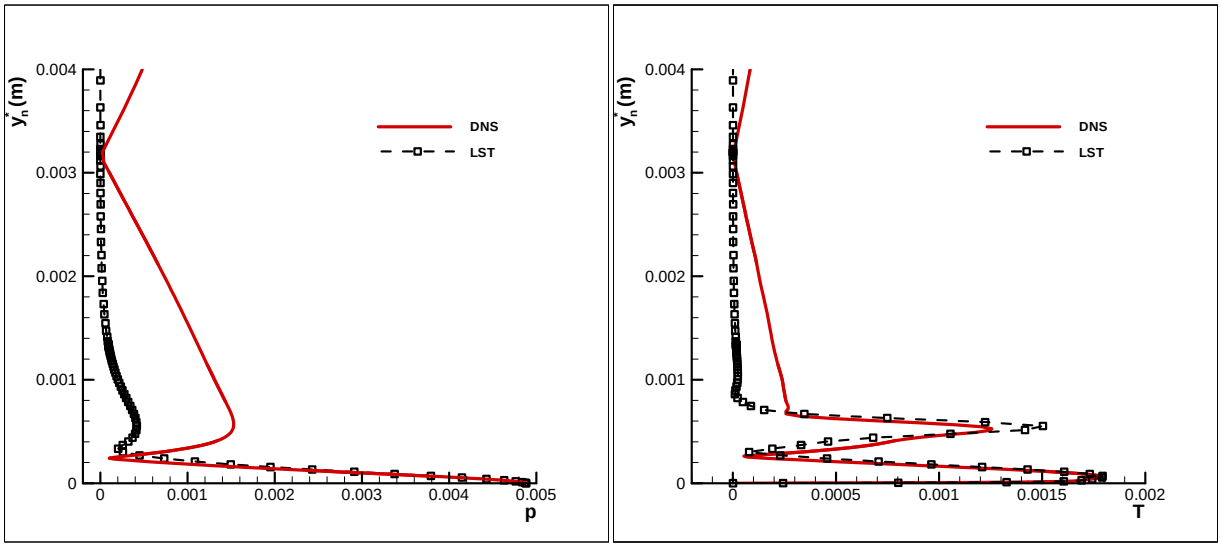

Figure 14. Comparison of amplitude distributions of pressure and temperature perturbations along the wall-normal direction at $s^* = 0.586\ m$ ***with*** $f_{13}^* = 683.121\ kHz$ ***for Case 1 of nose radius of 0.156 in.***

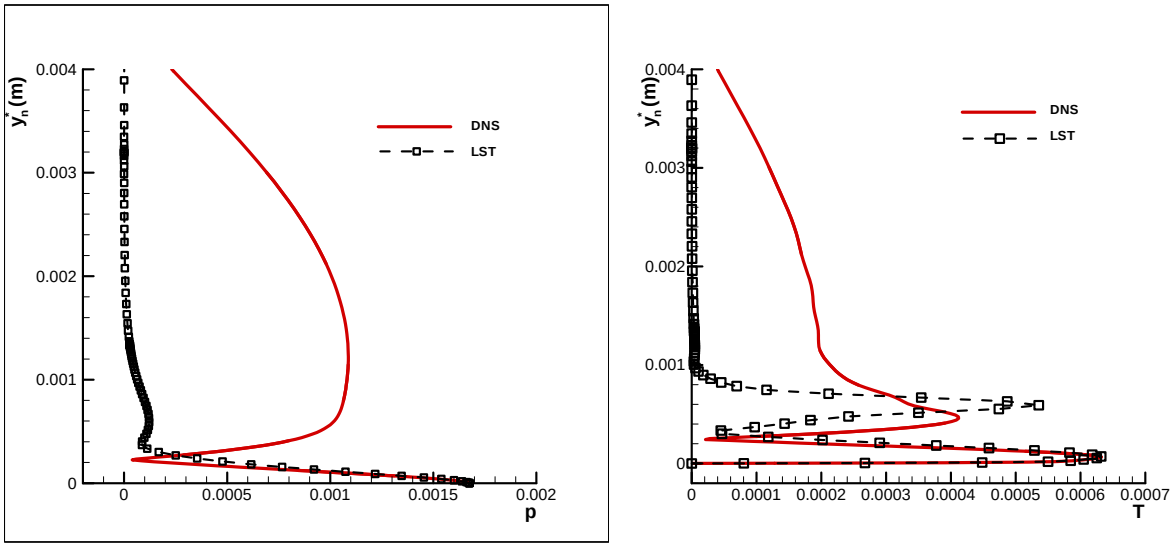

Figure 15. Comparison of amplitude distributions of pressure and temperature perturbations along the wall-normal direction at $s^* = 0.586\ m$ ***with*** $f_{12}^* = 630.610\ kHz$ ***for Case 1 of nose radius of 0.156 in.***

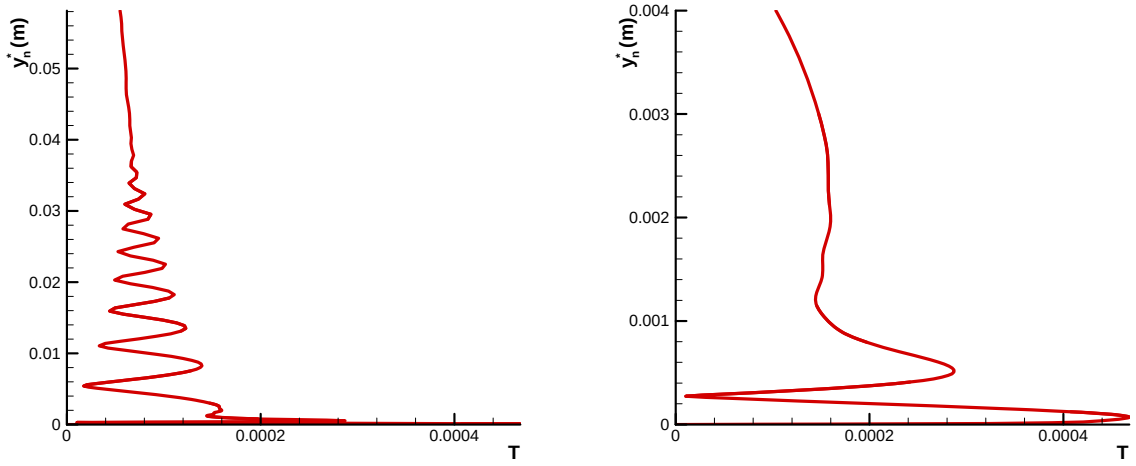

Figure 16. Amplitude distributions of temperature perturbations along the wall-normal direction at $s^* = 0.586\ m$ ***with*** $f_{11}^* = 578.060\ kHz$ ***for Case 1 of nose radius of 0.156 in. The right plot shows an enlarged local profile at the wall.***

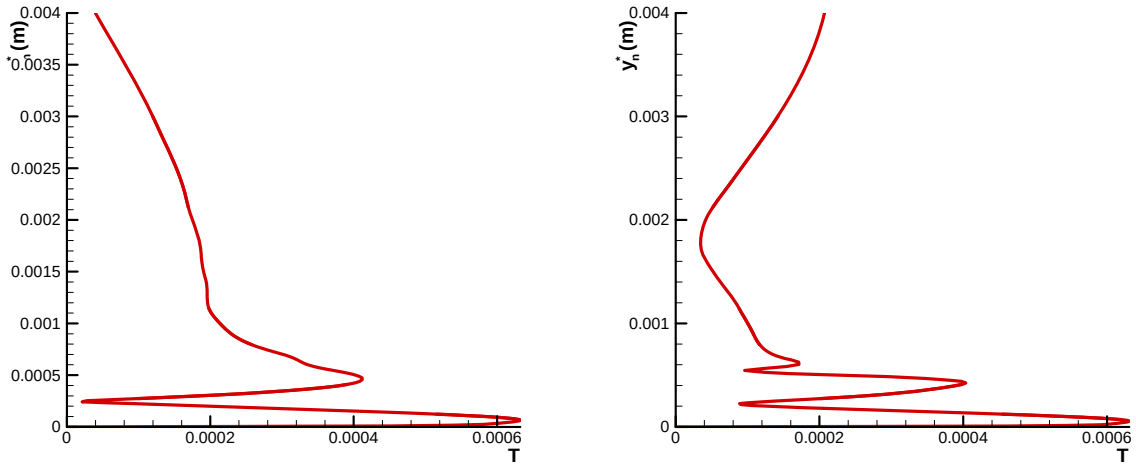

($f_{12}^* = 630.610\ kHz$) ($f_{14}^* = 735.712\ kHz$)

Figure 17. Amplitude distributions of temperature perturbations along the wall-normal direction at $s^* = 0.586\ m$ ***with two frequencies for Case 1 of nose radius of 0.156 in.***

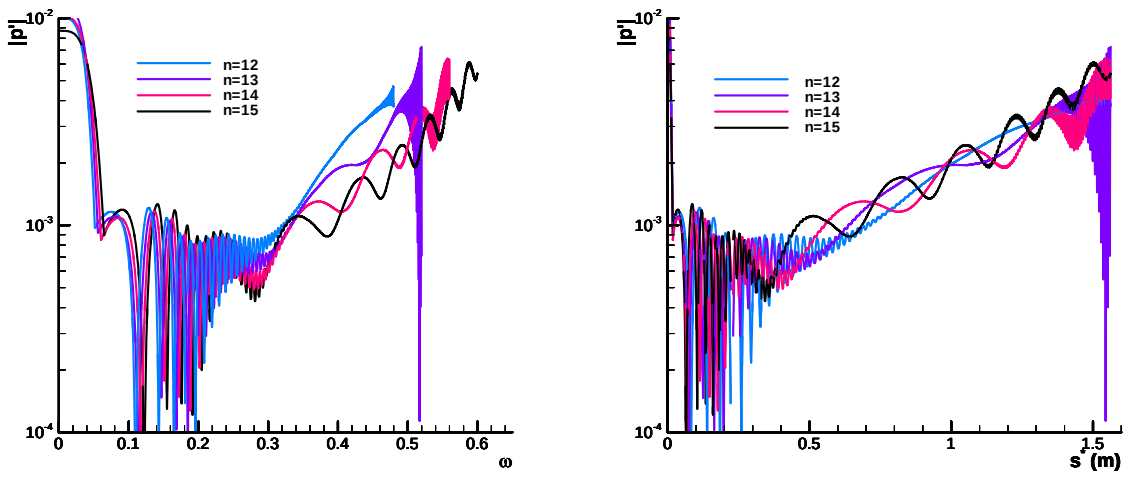

(a) **(b)**

Figure 18. Amplitude distributions of pressure perturbations as a function of (a) dimensionless frequency ω and (b) dimensional surface length. The lines represent different frequencies of $f_n^* = nf_1^*$, where $f_1^* = 32.114$ kHz for Case 2 of nose radius of 0.5 in.

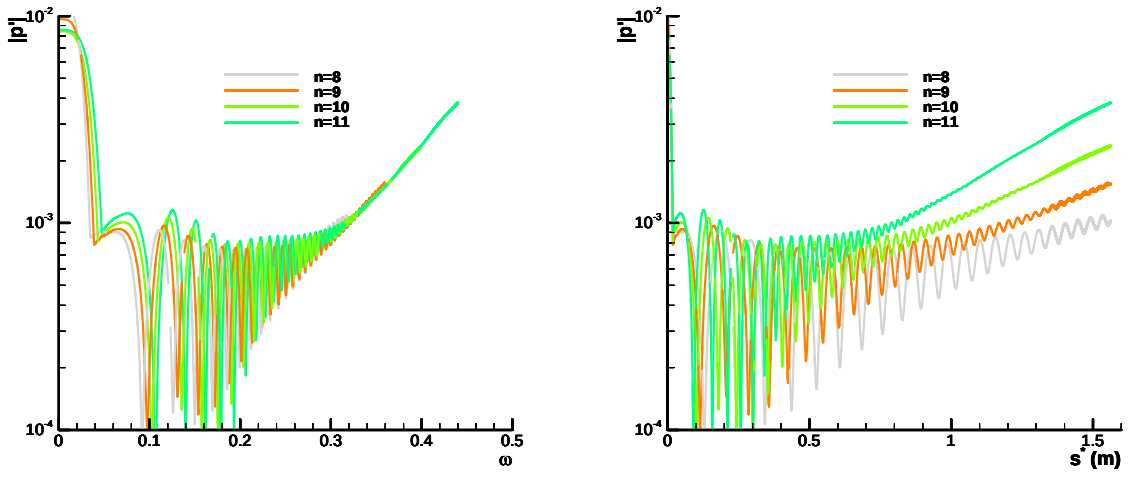

(a) **(b)**

Figure 19. Amplitude distributions of pressure perturbations as a function of (a) dimensionless frequency ω and (b) dimensional surface length. The lines represent different frequencies of $f_n^* = nf_1^*$, where $f_1^* = 32.114$ kHz for Case 2 of nose radius of 0.5 in.

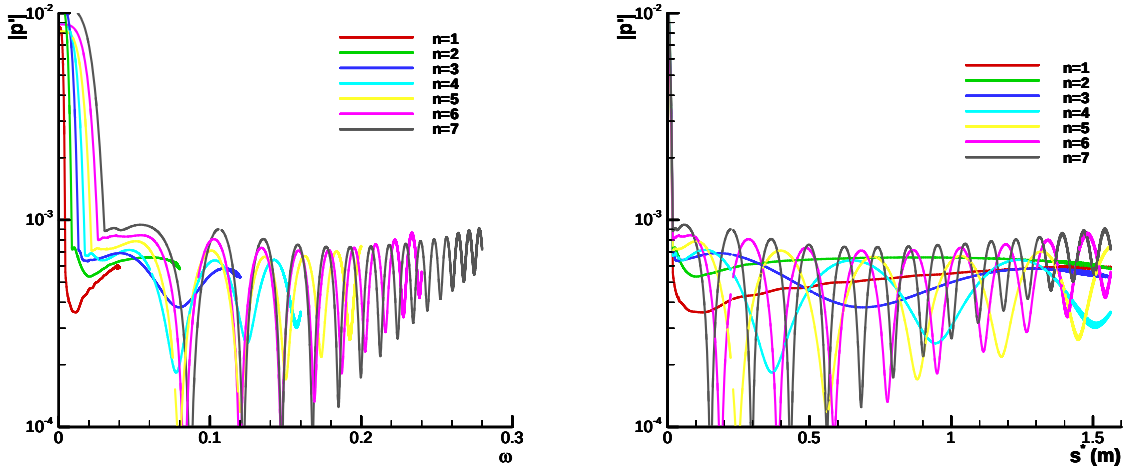

(a) **(b)**

Figure 20. Amplitude distributions of pressure perturbations as a function of (a) dimensionless frequency ω and (b) dimensional surface length. The lines represent different frequencies of $f_n^* = nf_1^*$, where $f_1^* = 32.114$ kHz for Case 2 of nose radius of 0.5 in.

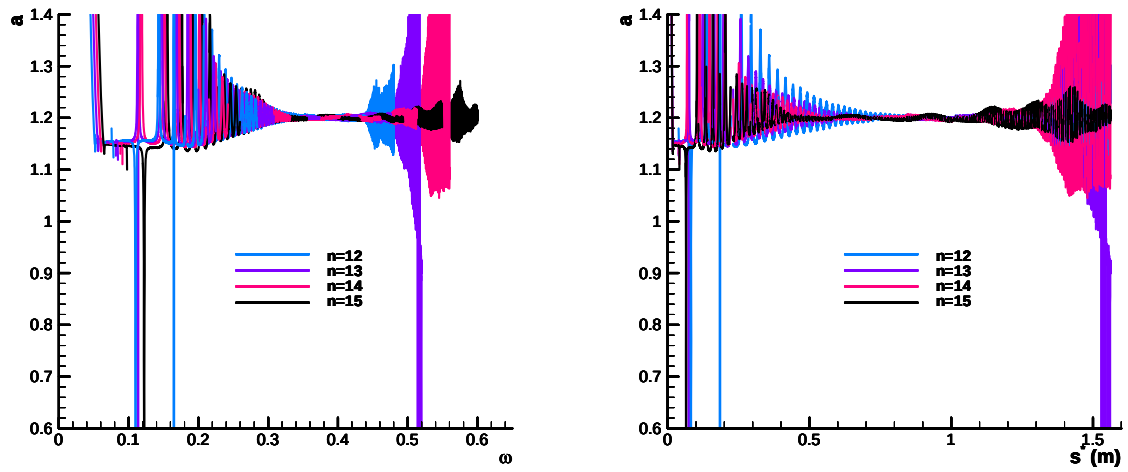

(a) **(b)**

Figure 21. Phase velocity distributions of pressure perturbations as a function of (a) dimensionless frequency ω and (b) dimensional surface length. The lines represent different frequencies of $f_n^* = nf_1^*$, where $f_1^* = 32.114$ kHz for Case 2 of nose radius of 0.5 in.

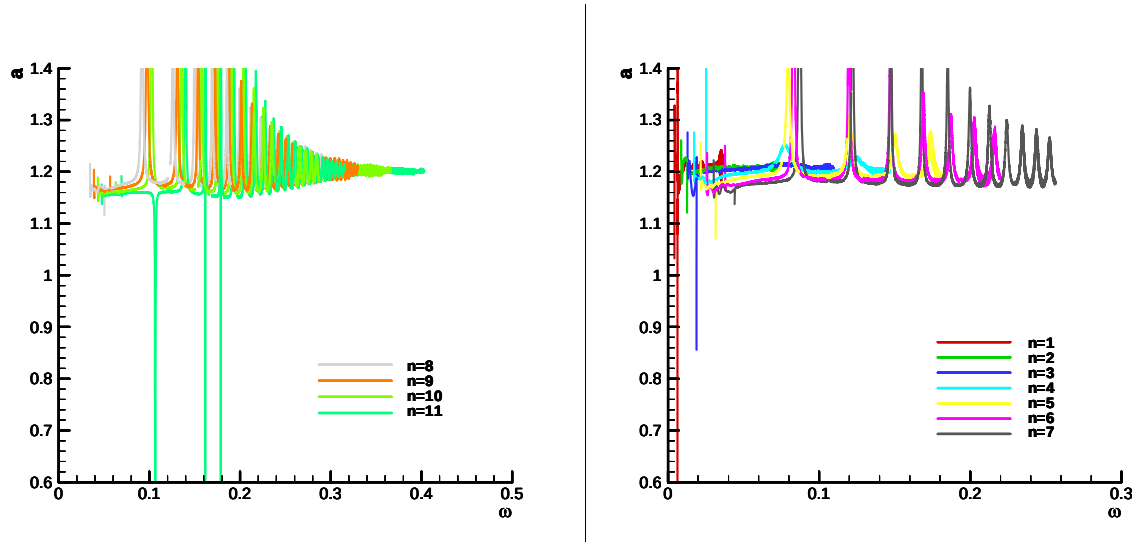

(a) **(b)**

Figure 22. Phase velocity distributions of pressure perturbations as a function of dimensionless frequency ω. The lines represent different frequencies of $f_n^* = nf_1^*$, where $f_1^* = 32.114$ kHz for Case 2 of nose radius of 0.5 in.

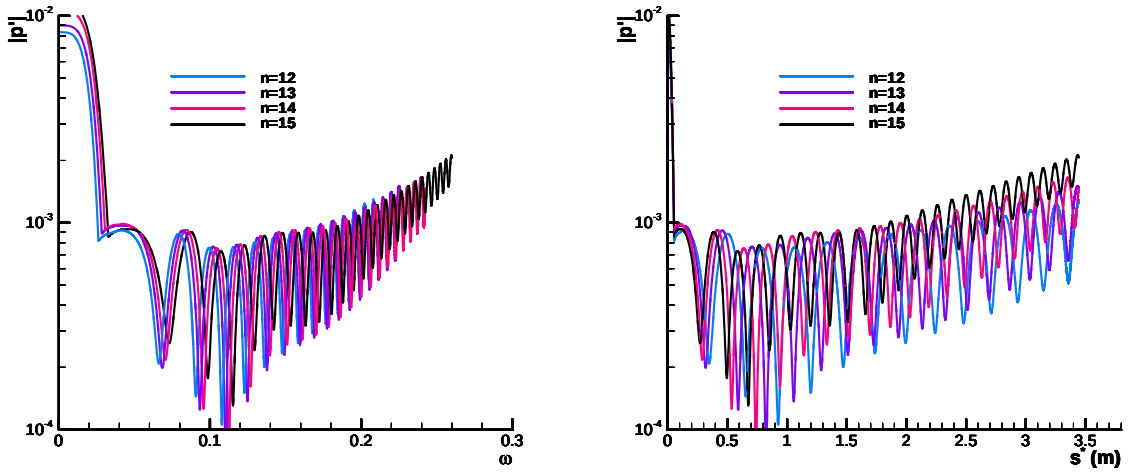

(a) **(b)**

Figure 23. Amplitude distributions of pressure perturbations as a function of (a) dimensionless frequency ω and (b) dimensional surface length. The lines represent different frequencies of $f_n^* = nf_1^*$, where $f_1^* = 20$ kHz for Case 3 of nose radius of 1.5 in.

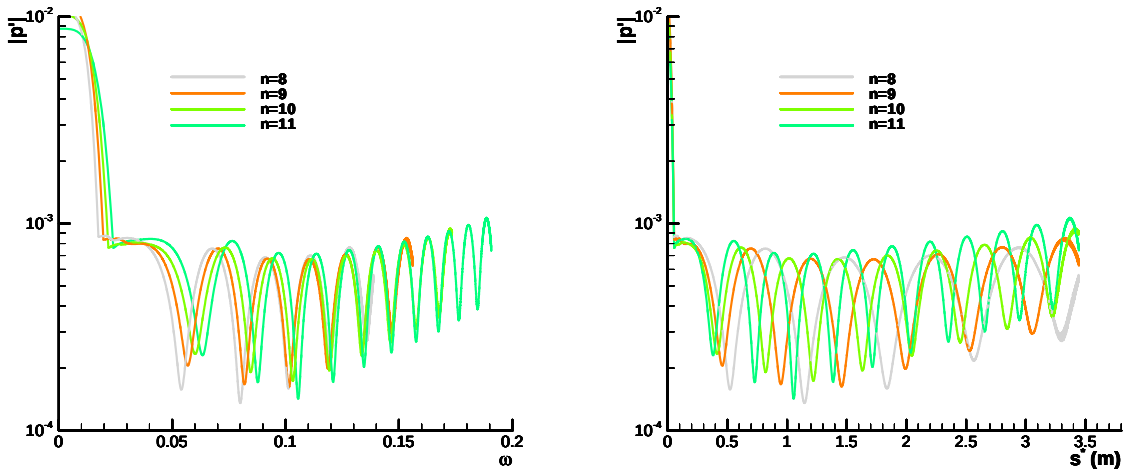

(a) **(b)**

Figure 24. Amplitude distributions of pressure perturbations as a function of (a) dimensionless frequency ω and (b) dimensional surface length. The lines represent different frequencies of $f_n^* = nf_1^*$, where $f_1^* = 20$ kHz for Case 3 of nose radius of 1.5 in.

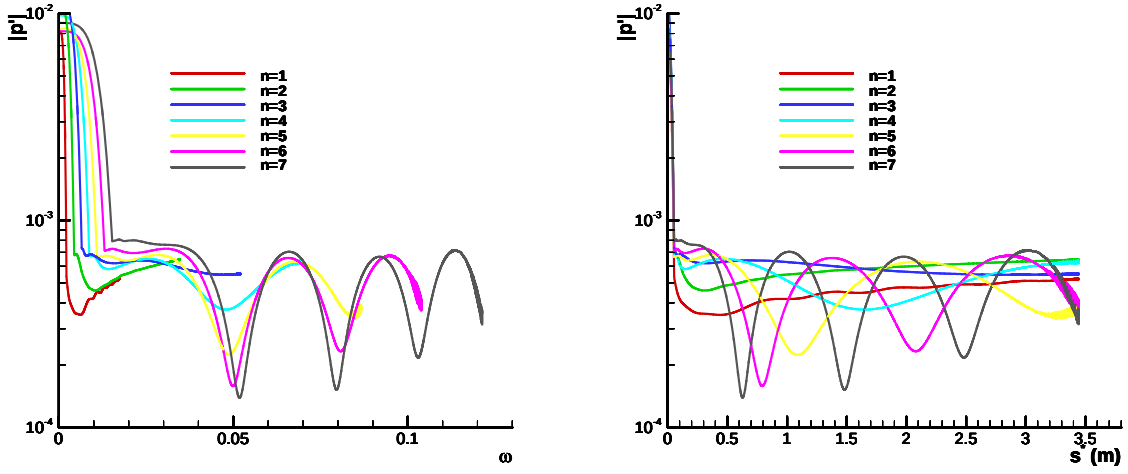

(a) **(b)**

Figure 25. Amplitude distributions of pressure perturbations as a function of (a) dimensionless frequency ω and (b) dimensional surface length. The lines represent different frequencies of $f_n^* = nf_1^*$, where $f_1^* = 20$ kHz for Case 3 of nose radius of 1.5 in.

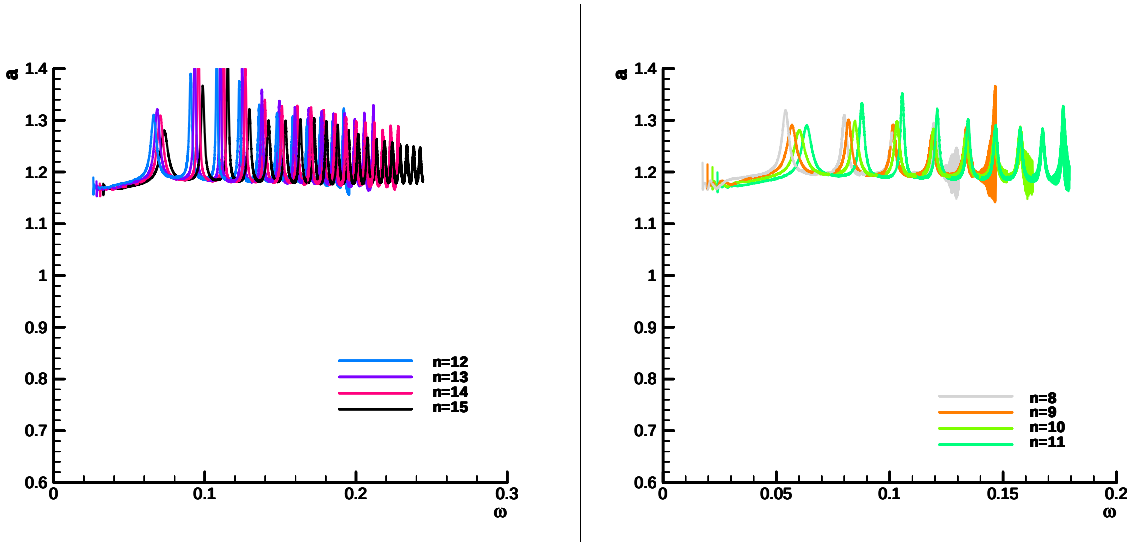

Figure 26. Phase velocity distributions of pressure perturbations as a function of dimensionless frequency ω. The lines represent different frequencies of $f_n^* = nf_1^*$, where $f_1^* = 20$ kHz for Case 3 of nose radius of 1.5 in.